

Data Repository Item 2009100

Seismic observation, receiver function imaging and reliability analysis

DR1. Seismic Observation and Receiver Functions Imaging

Seismic data used in this study were collected from the temporary stations of the North China Interior Structure Project (NCISP), which is a large seismic experiment carried out since 2000 for studying the tectonic evolution and the deep structures of North China (Zheng et al., 2005). For understanding the Proterozoic amalgamation of the Western and Eastern Blocks of the North China craton (NCC), a dense seismic array NCISP-4 crossing the Trans-North China orogen (TNCO) and the Western Block was deployed from September 2005 to September 2006. 50 temporary stations, numbered from 258 to 260, and 262 to 308, were emplaced with average spacing of ~10 km along an E-W transect, starting immediately to the west of the Hengshan massif in the TNCO, crossing the northern Ordos block, and ending at the western margin of the NCC (see Fig. 1 in the main text). All the stations were equipped with CMG-3ESP sensors (50Hz-30s) and Reftek 130-1 data acquisition systems. High-quality seismic data were acquired by the seismic experiment NCISP-4.

The receiver function imaging includes three processing steps. First, receiver functions were produced from the data at 49 stations in the NCISP-4 (station 264 was eliminated due to strong site noise) and 3 stations in the NCISP-2. Three-component seismograms were selected from 160 teleseismic events with body wave magnitude ≥ 5.5 and epicenter distance between 30° and 90° . The majority of the events concentrated within back-azimuth ranges of 40° - 60° and 110° - 200° . The waveforms were windowed from 20 s before and 100 s after the arrival time of the P wave, and the receiver functions were constructed using a time-domain maximum entropy deconvolution method (Wu and Zeng, 1998). A Gaussian parameter of 5 and a water level of 0.0001 were adopted in the deconvolution. Frequency content of our receiver functions from 0.05 Hz to 2.5 Hz allows for resolution of Ps phases from layer thicknesses of greater than 0.5 km. For most of the stations more than 50 receiver functions with high signal-to-noise ratio were selected after stringent visual inspection. The dataset contained 3183 receiver functions for further analysis. The station locations, and the numbers of receiver functions selected in each station are listed in Table S1.

To analyze the structural architecture presented by receiver functions, we performed Common Conversion Point (CCP) imaging (Zhu, 2000). We first calculated the ray-paths of receiver functions using a background velocity model. Each peak amplitude of receiver function was transferred to the corresponding locations along the ray-path where the P-to-S conversion occurred, using the time delay of conversion phase with respect to the direct P. This amplitude represents the velocity change, or more precisely the impedance change, of the medium at the

conversion point. We then divided the volume along the profile into certain sized bins and summed all amplitudes in each bin to obtain the average amplitude. The CCP imaging, based on an average crust-uppermost mantle model of the NCC (Zheng et al., 2006), reveals the major velocity discontinuities in the observed profile (Fig. S1a). It is noted that the Moho depth, derived from the first CCP imaging with an average crust model, is about 5 km deeper than that with the best-fitting model (Fig. S1b). However, the shape of velocity discontinuity is not sensitive to the models used in stacking.

To reconstruct the velocity structure in detail we used an integrated receiver functions imaging technique (Zheng et al., 2006) by iteratively implementing waveform inversion and CCP stacking of receiver functions. Due to the inherent trade-off between absolute seismic velocities and depths of discontinuities, the non-uniqueness of seismic inversion should be considered. The CCP depth image is helpful to assess the validity of the velocity structure model adopted in CCP stacking, and thus can be utilized to constrain the model space in waveform inversion of receiver functions. We implemented this idea by an iterating process seeking the optimal consistency of CCP image and waveform inversion result. In CCP stacking, the inverted velocity model from the preceding waveform inversion was applied to construct a depth image. The depth distributions (determined by the maximum amplitudes of the image) of the identified discontinuities in the CCP depth images were then utilized to constrain searching ranges of the corresponding layer thicknesses in the next inversion step; the inversion result was in turn applied as a new model for the CCP stacking of receiver functions. The misfit between CCP and waveform inversion was estimated by the standard deviation of the interface depth from the two methods. Such a two-step procedure was carried out iteratively until the inverted velocity model and the CCP depth image gave minimum misfit.

The synthetics were calculated based on a reflection matrix method (Kennett, 1983). An adapted hybrid global waveform inversion method (Liu et al., 1995; Ai et al., 1998) was used in the inversion process. The objective function in the inversion is defined by the degree of fit between synthetics and stacked receiver functions from data for both waveforms and amplitudes (Zheng et al., 2005). The best fitting model was searched from one dimensional models parameterized as a stack of layers for each station. The model parameters include shear wave velocity V_s , thickness, and V_p/V_s in each layer. The initial model framework is designed based on the interfaces identified from the CCP imaging. The searching ranges of model parameters in inversion were defined according to previous studies of the crustal structure in the eastern NCC (Zheng et al., 2006; 2007).

The best-fitting shear wave velocity models for all the 52 stations are shown in Fig. S2 with the corresponding synthetic receiver functions also plotted superposed upon the data. The model parameters of the inverted velocity structures above 60 km depth are listed in Table S2.

DR2. Reliability Analysis

The integrated receiver function imaging technique used in this study involves CCP stacking and waveform inversion of receiver functions that provide complementary constraints

on the crustal structures. CCP stacking is performed based on the travel-times of converted waves and thus gives depth information of velocity discontinuities; waveform inversion, on the other hand, relies on the amplitudes and shapes of the seismic signals and aims to retrieve velocity variations across the discontinuities. Both techniques, however, suffer from certain intrinsic problems. For instance, the time-to-depth transfer of CCP stacking is strongly dependent on the velocity model, whereas the inversion result is strongly non-unique. By combining and seeking consistent results from these two methods, the quality of the structural image is expected to be improved considerably.

We calculated the standard deviation of interface depth to estimate the misfit of the CCP image and the velocity interfaces obtained from the inversion. The average depths of crustal interfaces obtained from the CCP imaging and the inverted velocity model, as well as their standard deviation are listed in Table S3. The values of standard deviation of the depth are less than 1 km for the crustal interfaces except the bottom-interface of the low-velocity layer in the lower-crust. For the latter the interfaces were locally close to the Moho and resulted in uncertainty of identifying depth in the CCP image.

In our receiver function inversion, assessment of the match between the calculated and observed receiver functions is provided by the minimization of an objective function. To further estimate the uncertainties of model parameters, especially considering the trade-off between absolute velocities and depths, we designed a space of velocity models by changing shear wave velocity ± 0.4 km/s with 0.1 km/s interval and layer thickness ± 1.0 km with 0.1 km interval around the values of the inverted best-fitting model. Outside the parameter space with shear wave velocity change of ± 0.1 km/s and layer thickness change of ± 0.5 km, only 549 models (7.8%) have values of the objection function less than that of the final model. Based upon the ranges of parameter spaces of the 549 models, it can be estimated that the resolution of shear wave velocity is ± 0.1 km/s, and the resolution of depth is ± 0.5 km for 92.2% reliability in the waveform inversion. These synthetic tests therefore indicate the high reliability of the final velocity models.

References Cited

- Ai, Y., Liu, P., and Zheng, T.Y., 1998, Adaptive hybrid global inversion algorithm: *Scientia Sinica (B)*, v. 41, p. 137-143.
- Kennett, B.L.N., 1983, *Seismic Wave Propagation in Stratified Media*: Cambridge University Press, Cambridge, p. 231-273.
- Liu, P., Hartzell, S., and Stephenson, W., 1995, Non-linear multiparameter inversion using a hybrid global search algorithm, applications in reflection seismology: *Geophys. J. Int.*, v. 122, p. 991-1000.
- Wu, Q.J., and Zeng, R.S., 1998, The crustal structure of Qinghai-Xizang plateau inferred from broadband teleseismic waveform: *ACTA Geophysica Sinica*, v.41, p.669-679 (in Chinese).
- Zheng T.Y., Zhao, L., and Chen, L., 2005, A detailed receiver function image of the sedimentary structure in the Bohai Bay Basin: *Phys. Earth Planet. Inter.*, v. 152, p. 129-143 ,

doi:10.1016/j.pepi.2005.06.011.

Zheng T.Y., Chen, L., Zhao, L., Xu, W.W., and Zhu, R.X., 2006, Crust-mantle structure difference across the gravity gradient zone in North China Craton: Seismic image of the thinned continental crust: *Phys. Earth Planet. Inter.* v. 159, p. 43-58, doi:10.1016/j.pepi.2006.05.004..

Zheng T.Y., Chen, L., Zhao, L., and Zhu, R.X., 2007, Crustal structure across the Yanshan belt at the northern margin of the North China Craton: *Phys. Earth Planet. Inter.*, v. 161, p. 36-49, doi:10.1016/j.pepi.2007.01.004..

Zhu, L., 2000, Crustal structure across the San Andreas Fault, Southern California from teleseismic converted waves: *Earth Planet. Sci. Lett.*, v.179, p.183-190, doi: 10.1016/S0012-821X(00)00101-1.

Table DR1. Seismic stations for which receiver function analysis and inversion were carried out, including the number of the receiver functions selected for each station.

| Station | Longitude (E) | Latitude (N) | Number of receiver functions |
|---------|------------------|------------------|---------------------------------|
| 197 | 113°46'17" | 39°48'37" | 64 |
| 199 | 113°36'13" | 39°55'04" | 73 |
| 200 | 113°29'40" | 39°57'10" | 67 |
| 258 | 113°13'08" | 39°48'22" | 98 |
| 259 | 113°01'19" | 39°48'50" | 69 |
| 260 | 112°53'10" | 39°47'45" | 52 |
| 262 | 112°44'38" | 39°47'33" | 54 |
| 263 | 112°37'34" | 39°47'06" | 35 |
| 265 | 112°22'57" | 39°45'59" | 58 |
| 266 | 112°15'00" | 39°46'44" | 22 |
| 267 | 112°07'48" | 39°45'36" | 42 |
| 268 | 112°00'25" | 39°44'09" | 63 |
| 269 | 111°53'24" | 39°45'36" | 33 |
| 270 | 111°45'00" | 39°45'36" | 69 |
| 271 | 111°39'00" | 39°45'00" | 71 |
| 272 | 111°33'00" | 39°45'00" | 57 |
| 273 | 111°25'48" | 39°44'24" | 42 |
| 274 | 111°16'48" | 39°44'24" | 38 |
| 275 | 111°10'48" | 39°43'12" | 55 |
| 276 | 111°03'36" | 39°43'12" | 86 |
| 277 | 110°57'00" | 39°43'12" | 91 |
| 278 | 110°50'24" | 39°42'00" | 72 |
| 279 | 110°43'12" | 39°41'24" | 23 |
| 280 | 110°37'12" | 39°42'00" | 38 |
| 281 | 110°29'12" | 39°40'48" | 32 |
| 282 | 110°21'00" | 39°41'24" | 62 |
| 283 | 110°15'00" | 39°40'48" | 24 |
| 284 | 110°07'48" | 39°40'12" | 40 |
| 285 | 110°00'36" | 39°40'12" | 63 |
| 286 | 109°52'48" | 39°40'48" | 73 |
| 287 | 109°46'12" | 39°39'00" | 56 |
| 288 | 109°37'12" | 39°39'00" | 72 |
| 289 | 109°32'24" | 39°39'00" | 65 |
| 290 | 109°25'12" | 39°38'24" | 70 |

| | | | |
|-----|------------|-----------|----|
| 291 | 109°18'00" | 39°37'12" | 76 |
| 292 | 109°12'00" | 39°37'12" | 73 |
| 293 | 109°04'12" | 39°37'12" | 80 |
| 294 | 108°57'36" | 39°37'12" | 63 |
| 295 | 108°50'24" | 39°37'12" | 67 |
| 296 | 108°42'36" | 39°36'36" | 70 |
| 297 | 108°36'00" | 39°37'12" | 73 |
| 298 | 108°28'48" | 39°36'00" | 80 |
| 299 | 108°22'12" | 39°36'00" | 76 |
| 300 | 108°13'48" | 39°35'24" | 30 |
| 301 | 108°07'12" | 39°35'24" | 91 |
| 302 | 108°00'36" | 39°34'48" | 70 |
| 303 | 107°53'24" | 39°34'48" | 78 |
| 304 | 107°47'24" | 39°33'36" | 80 |
| 305 | 107°39'36" | 39°33'36" | 75 |
| 306 | 107°32'24" | 39°34'12" | 25 |
| 307 | 107°26'24" | 39°33'00" | 69 |
| 308 | 107°16'48" | 39°34'12" | 78 |

Table DR2. Vp, Vs, density, and layer thickness of the best-fitting models obtained by waveform inversion

| Layers | Vp (km/s) | Vs (km/s) | Density (g/cm ³) | Average thickness (km) |
|-----------------------------------|----------------|----------------|---------------------------------|------------------------------|
| Sediment | 3.22-5.40 | 1.66-2.92 | 2.10-2.57 | 2.5 |
| Upper-Crust | 6.05-6.18 | 3.49-3.55 | 2.64-2.75 | 3.0 |
| Middle-Crust | 6.31-6.54 | 3.65-3.75 | 2.79-2.86 | 9.1 |
| Lower-crust | 6.57-6.75 | 3.80-3.90 | 2.86-2.93 | 27.0 |
| low-velocity dipping layer | 6.26 | 3.60-3.70 | 2.82 | 9.7 |
| low-velocity layer in lower-crust | 6.47 | 3.70 | 2.86 | 10.0 |
| Crust-mantle transition zone | 7.00-7.57 | 4.00-4.30 | 3.01-3.19 | 2.8 |
| Uppermost mantle | 7.74-8.37 | 4.40-4.70 | 3.25-3.44 | / |

Table DR3. Average depth of the velocity interfaces obtained from the CCP image and the inverted velocity model and the standard deviation between them

| Velocity interfaces | Average depth (km) | | Relative error (%) | Standard deviation (km) |
|--|---------------------------|------------------|-----------------------------------|--|
| | CCP image | inversion | | |
| Upper-middle Crust | 5.37 | 5.52 | 2.94 | 0.71 |
| Middle-lower Crust | 12.34 | 12.47 | 1.01 | 0.71 |
| Moho | 41.44 | 41.64 | 0.47 | 0.59 |
| upper-interface of low-velocity dipping layer | 10.36 | 10.27 | 0.83 | 0.56 |
| bottom-interface of low-velocity dipping layer | 19.76 | 20.00 | 1.21 | 0.87 |
| upper-interface of low-velocity layer in lower-crust | 24.87 | 24.85 | 0.06 | 0.93 |
| bottom-interface of low-velocity layer in lower-crust | 35.27 | 34.82 | 1.29 | 1.84 |

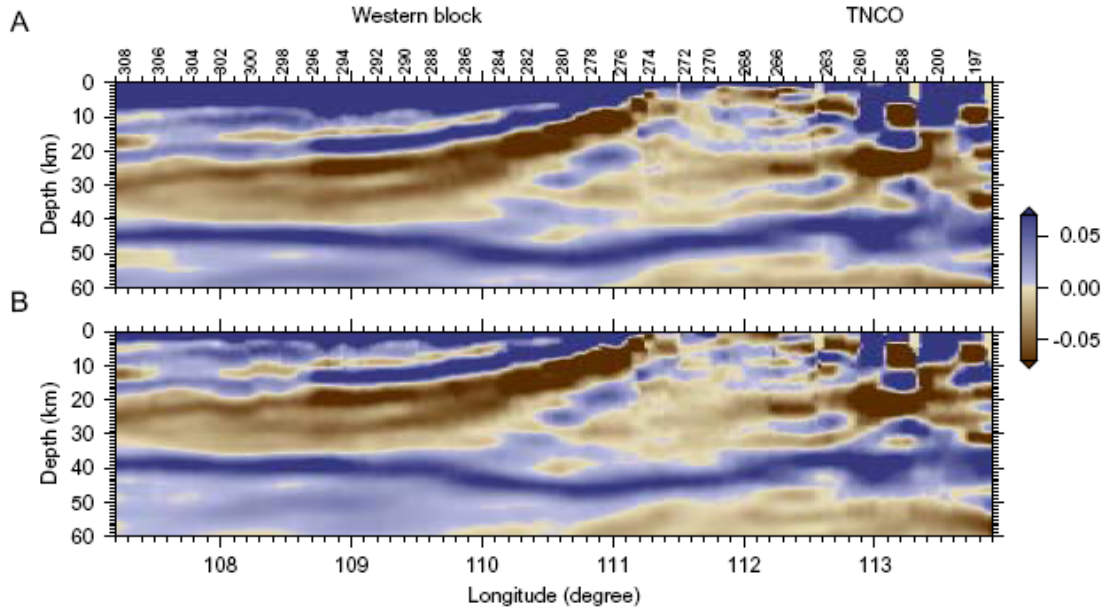


Figure DR1. A: CCP image based on an average crust-uppermost mantle model of the NCC, in which selected station numbers are labeled on the top of the plot, and B: based on the final model obtained from the waveform inversion. Blue (brown) color represents positive (negative) amplitude of the receiver function, indicating velocity increase (decrease) downwards.

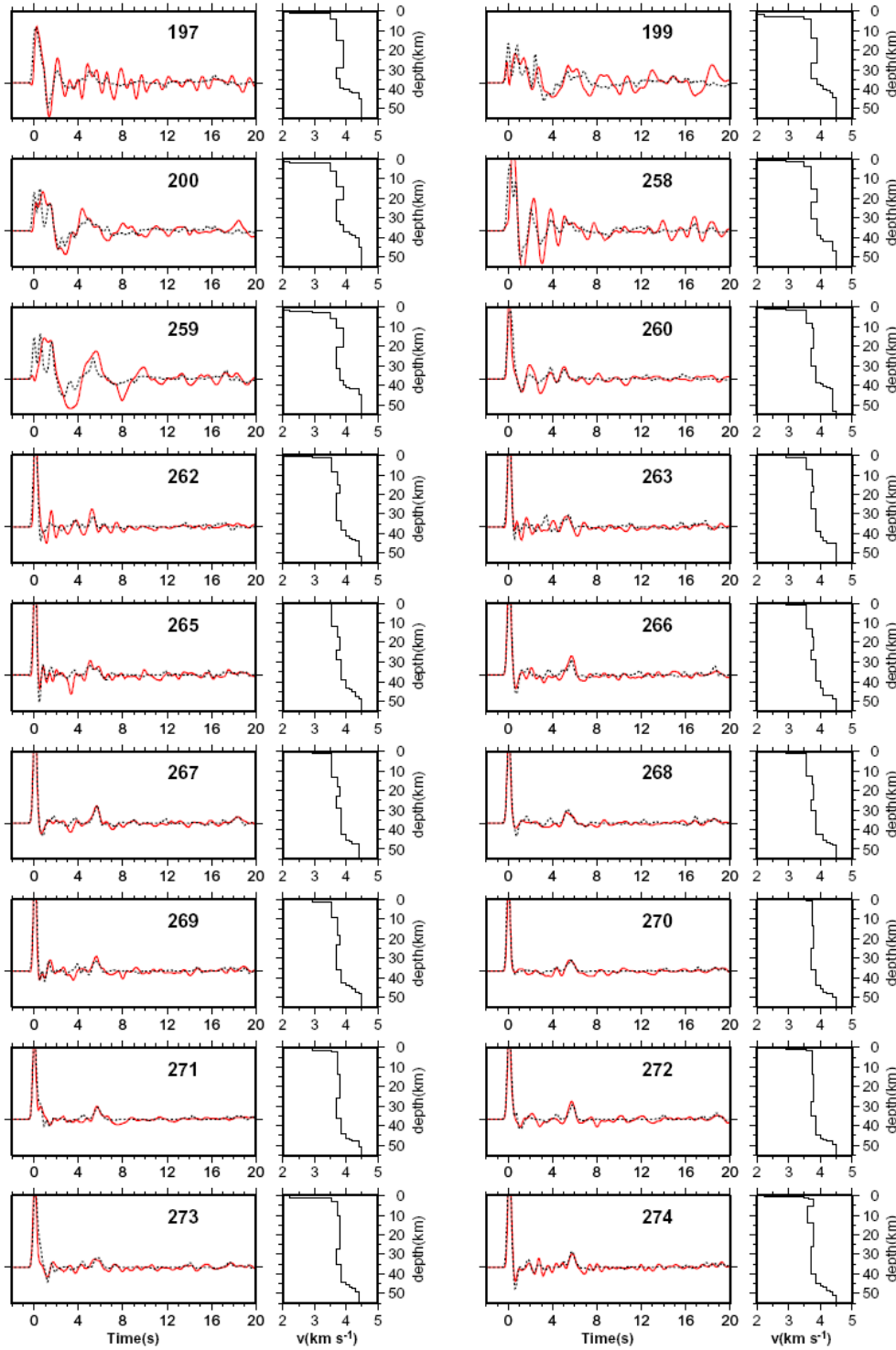


Figure DR2. Shear-wave velocity models and comparisons between synthetics and observed receiver functions for all the 49 stations. For each station the best-fitting shear-wave velocity model is plotted in the right panel, the receiver functions are plotted in the left panel with data in red line and synthetic in dotted line. The station numbers are marked in the left panels.

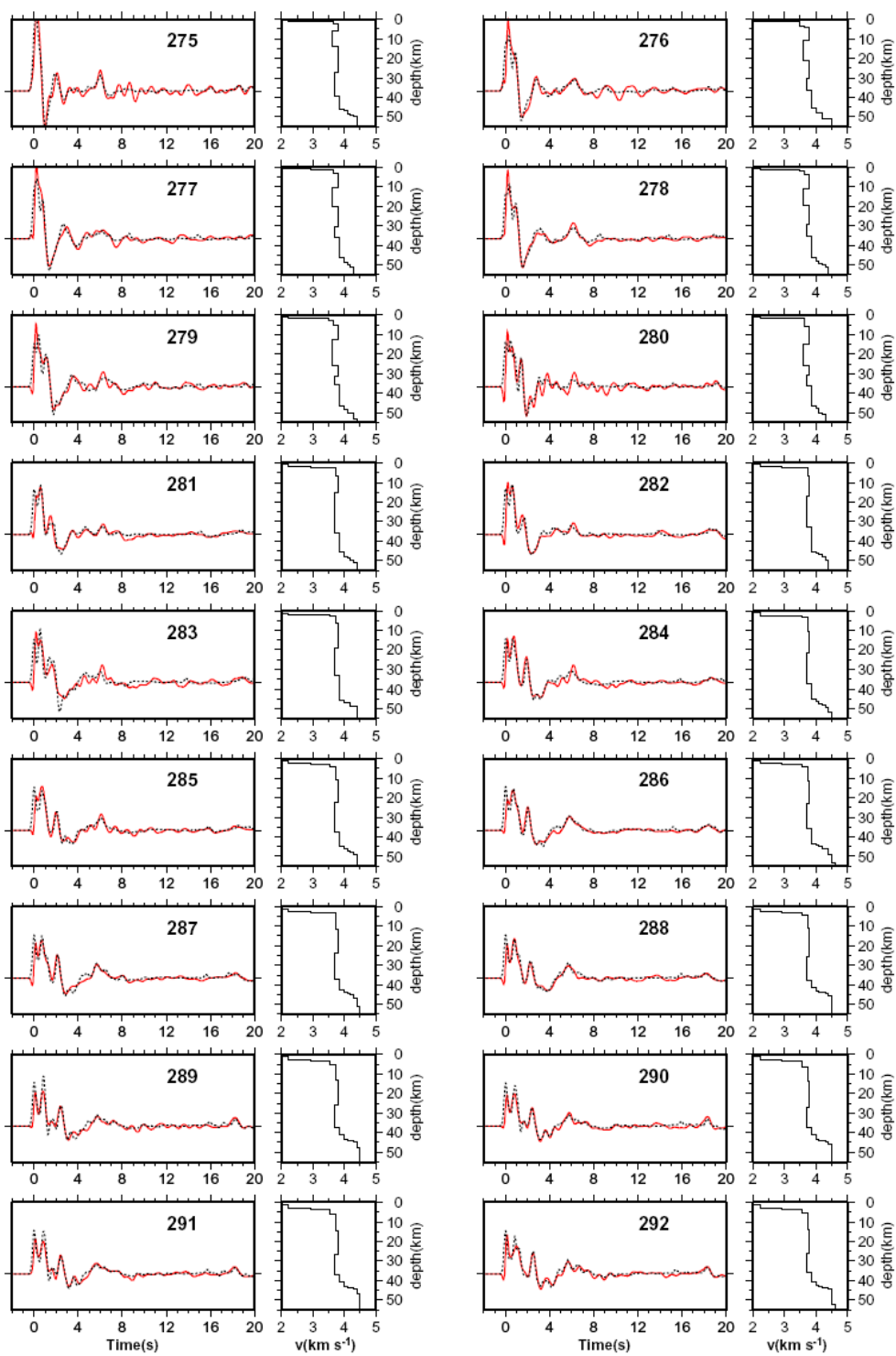


Fig. DR2 (continued)

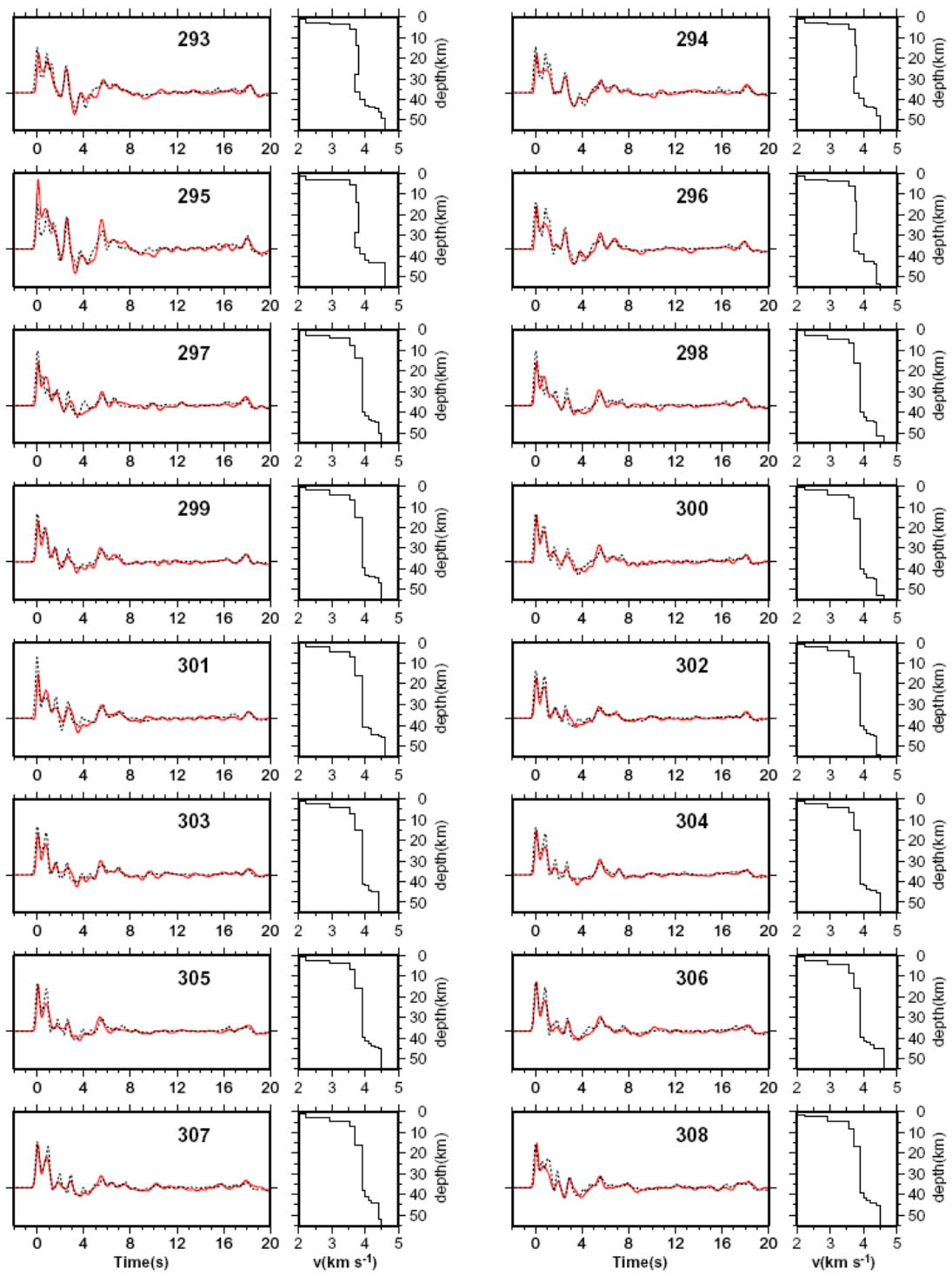


Fig. DR2 (continued)